Digest Journal of Nanomaterials and Biostructures Vol. 20, No. 4, October-December 2025, p. 1665-1673

Solution combustion-synthesised MoO_3 nanoparticles for dual photo-catalytic and antibacterial applications in sustainable agriculture

S. Jeyani Shalu *, R. S. Rimal Isaac
[a] *Department of Nanotechnology, Noorul Islam Centre for Higher Education, Kumaracoil, Thuckalay-629 180, Tamilnadu, India*

Molybdenum trioxide nanoparticles were synthesised via a simple and cost-effective solution combustion method. XRD confirmed an orthorhombic crystalline phase with an average crystalline size of 56.6 nm. UV-Vis spectroscopy indicated a direct bandgap of 2.9 eV, while RAMAN spectra revealed Mo = O and Mo-O stretching vibrations. SEM-EDAX analysis confirmed nanoscale morphology and a uniform Mo-O distribution. Photocatalytic studies, under direct sunlight, degraded 92% methylene blue dye within 120 min, following pseudo-first-order kineticsS. Furthermore, dose-dependent antibacterial activity was exhibited against *E. coli* and *S. aureus*. These findings highlight MoO_3 NPs for sustainable agriculture by degrading pollutants and controlling microbes in irrigation systems.

(Received October 7, 2025; Accepted December 29, 2025)

Keywords: MoO_3 nanoparticles, Solution combustion synthesis, Photocatalysis, Antibacterial activity, Sustainable agriculture

1. Introduction

Nanotechnology has rapidly emerged as a leading research field, offering innovative strategies for fabricating functional materials with applications in catalysis, drug delivery, environmental remediation, agriculture, energy storage, sensor technologies, and biomedicine [1, 2]. Transition metal oxides are widely studied for their tunable band gaps, high surface areas, and reactive oxygen species (ROS) generation, making them excellent candidates for photocatalysis and antimicrobial applications [3, 4].

Molybdenum trioxide nanoparticles (MoO3 NPs) are wide-band-gap semiconductors (2.7 to 3.8 eV) with excellent structural stability, high oxidising potential, and chemical robustness [5]. These properties make them suitable for applications in Photocatalysis, gas-sensing, electrochromic devices, and antimicrobial coatings [6, 7]. Recent studies indicate that MoO3 NPs can effectively degrade organic dyes and inhibit microbial growth through ROS-mediated mechanisms [8–10]. Such multifunctional properties render them valuable for environmental and biological applications.

Agricultural productivity is increasingly challenged by the excessive use of agrochemicals, such as pesticides and fertilisers, which lead to soil and water contamination [11, 12]. In addition, pathogenic bacteria, including Escherichia coli and Staphylococcus aureus, pose a threat to crop yield and food safety [13, 14]. Conventional remediation strategies are often inefficient, costly, or environmentally harmful. Developing a single nanomaterial capable of simultaneously degrading chemical pollutants and controlling microbial growth offers a sustainable approach for improving water quality and crop protection [15, 9].

Among various synthesis techniques, the combustion method provides a rapid, cost-effective, and energy-efficient route to produce metal oxide NPs with high crystallinity and large surface areas. Comparing hydrothermal and sol-gel approaches, combustion synthesis allows faster processing and greater scalability [16].

* Corresponding author: jeyanishalu@niuniv.com
https://doi.org/10.15251/DJNB.2025.204.1665

In this study, MoO3 NPs were synthesised via the combustion method and characterised using XRD, UV-Vis spectroscopy, Raman spectroscopy, and SEM-EDAX. The breakdown of methylene blue, used as a reference organic pollutant, was monitored to evaluate photocatalytic efficiency, while antibacterial activity was evaluated against Gram-positive and Gram-negative bacteria.

2. Experimental Section

2.1 Synthesis of MoO3 Nanoparticles

MoO3 NPs were synthesised using the Solution Combustion Synthesis (SCS) method. Ammonium heptamolybdate tetrahydrate ((NH4)6Mo7O24.4H2O) (1g) was used as the precursor. Calcination was carried out at 600℃ for 1 hr using a muffle furnace [17]. The precursor thermally decomposed to yield MoO3 NPs as shown below:

$$(NH_4)_6Mo_7O_{24}.4H_2O \xrightarrow{600℃} 7MoO_3 + 6NH_3 \uparrow + 7H_2O \uparrow$$

After calcination, the nano powder was cooled to ambient temperature and subsequently kept in an Eppendorf tube for further use.

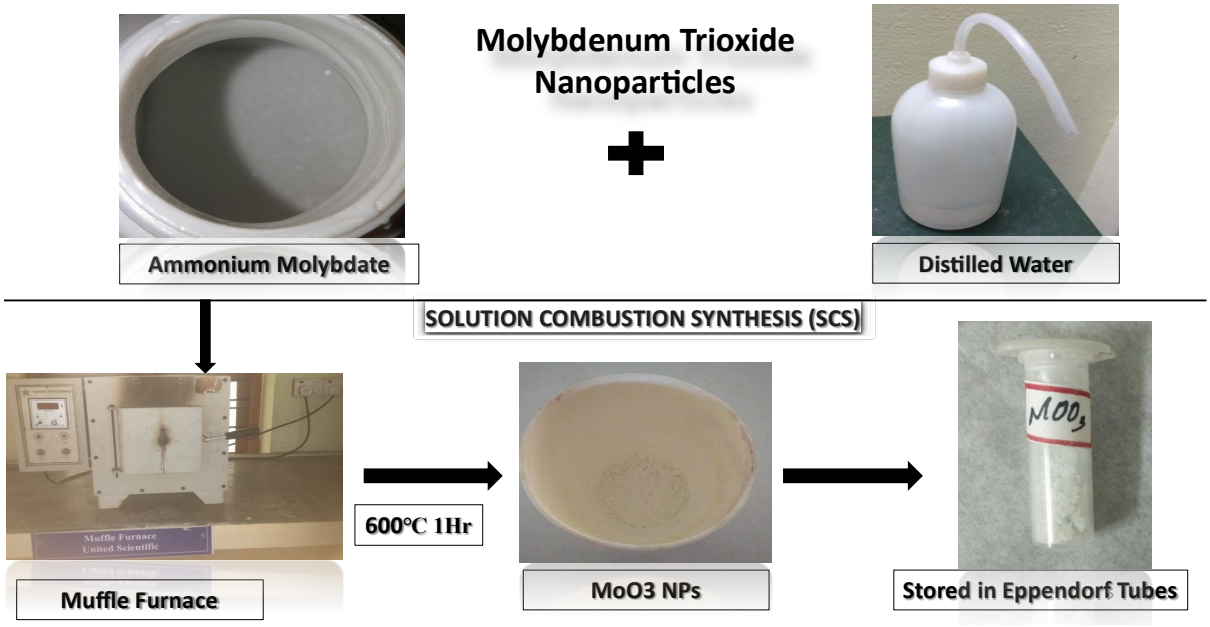

Fig. 1. Solution Combustion Synthesis (SCS) of MoO_3 NPs.

2.2 Characterisation of MoO3 Nanoparticles

XRD analysis was performed using a Bruker D2 Phaser diffractometer. UV-Vis spectra were recorded with a Systronics 2202 spectrophotometer (India). Raman spectra were obtained using an EZRaman system (Enwave Optronics, USA). SEM-EDAX analysis was carried out at 2000x magnification and 20 kV using a CARL ZEISS EVO 18 model.

2.3 Procedure of photocatalytic experiment

For the photocatalytic degradation study, 10 mg/L Methylene blue (MB) solution and 0.1 g of MoO3 NPs were added to 100 mL of Distilled water. The mixture was then exposed to direct sunlight, and 5 mL aliquots were withdrawn at 20-minute time intervals. Each aliquot was centrifuged at 5000 rpm for 10 minutes to separate MoO3 NPs, and the absorbance of the obtained supernatant was recorded at 664nm using a Systronics 2202 UV-Vis spectrophotometer.

The efficiency of photocatalytic degradation was determined using the formula:

$$Degradation\ efficiency\ (\%)\ = \frac{C_0 - C_t}{C_0} \times 100 \quad (1)$$

C_0: Initial dye concentration (mg/L).
C_t: Dye concentration at irradiation time t (mg/L) [18].

2.4 Procedure of antibacterial activity

2.4.1 Test Organisms

Bacterial strains used for antibacterial testing, Escherichia coli and Staphylococcus aureus, were sourced from Microbial Type Culture Collection and Gene Bank (MTCC), Chandigarh, and maintained on Nutrient Agar (NA).

2.4.2 Nutrient Broth Preparation

Pure cultures were streaked onto a Nutrient Agar plate and maintained for 24 h at 37 °C. Fresh cultures were inoculated into sterile 0.145 M saline (2 ml), and the cellular count was adjusted to 0.5 McFarland turbidity, yielding a concentration of 1.5×108 CFU/ml [19]. This standardised suspension was employed for antibacterial studies.

2.4.3 Antibacterial Test

Mueller-Hinton Agar (38 g/L) was dispersed in distilled water and autoclaved at 250 ℉ under 15 psi for 15 min (pH 7.3). The media was cooled, mixed thoroughly, and dispersed at 25 mL per Petri plate. Plates were subsequently streaked with cultures of the pathogenic bacteria, Escherichia coli and Staphylococcus aureus. Ciprofloxacin (5 µg) discs served as Positive controls, and empty sterile discs as negative controls. Sterile discs (6 mm) were prepared by pipetting varying concentrations of the test sample onto them. After incubation for 24 h at 37°C, the diameters of growth inhibition zones (including disc) were measured in millimetres using a transparent ruler [20–22].

2.5 Statistical analysis

The study included three independent replicates for each test, and the mean ± SD was used to quantify the overall findings. The photocatalytic degradation efficiency was analysed by plotting C/C0 versus irradiation time and fitting the data with a pseudo-first-order kinetic model (ln(C0/C) = kt). Statistical significance of experimental results was determined using one-way (ANOVA), with $p < 0.05$ considered significant.

3. Result and Discussion

3.1 X-ray diffraction analysis

XRD pattern for the synthesised MoO3 NPs is shown in Figure 2, which is in accordance with the (JCPD card no. 05-0508). The reflections observed at 23.3˚,25.7˚,27.3˚,28.3˚, and 33.6˚, which correspond to the (022), (211), (170), (080), and (171) planes of orthorhombic α-MoO3 NPs correspond to lattice parameters (a = 3.962 Å, b = 13.858 Å, c = 3.697Å). The sharp and intense peaks confirm the crystalline structure, with a degree of crystallinity of 82.1 %. Using the Debye-Scherrer method, the calculated average crystalline size was 56.6 nm.

$$D\ = \frac{K\lambda}{\beta cos\theta} \quad (2)$$

D: Crystalline size of nanoparticles,
K: Scherrer constant (0.98),
λ: wavelength (1.54)
β: Full width at half maximum (FWHM)
Absence of any secondary peaks confirmed its phase purity [23].

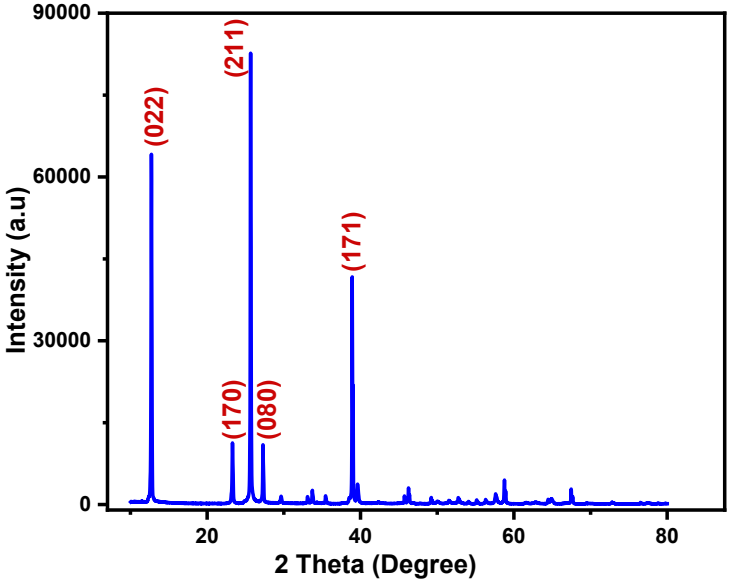

Fig. 2. XRD pattern of MoO_3 nanoparticles synthesised by the solution combustion method.

3.2 UV-visible spectroscopy

The UV-Visible analysis for the synthesised MoO3 NPs are shown in Figure 3a. It exhibited a strong absorption band at 240nm, confirming the formation of MoO3 NPs.The peak is due to d-d transitions of Mo6+ ions in the oxide lattice [24]. Tauc's method was employed to estimate the optical band gap (Eg) of the synthesised MoO3 NPs. As shown in Figure 3b, $(\alpha h\nu)^2$ is plotted against photon energy $(h\nu)$ For direct transitions. According to the Tauc equation:

$$(\alpha h\nu)^n = \mathrm{A}(h\nu - E_g) \qquad (3)$$

Where,

A: proportionality constant

n: electronic transition(n = 2 for direct, n = $\frac{1}{2}$ for indirect).

The bandgap of 2.9 eV was determined using the x-axis intercept from the linear fit of the plot [25].

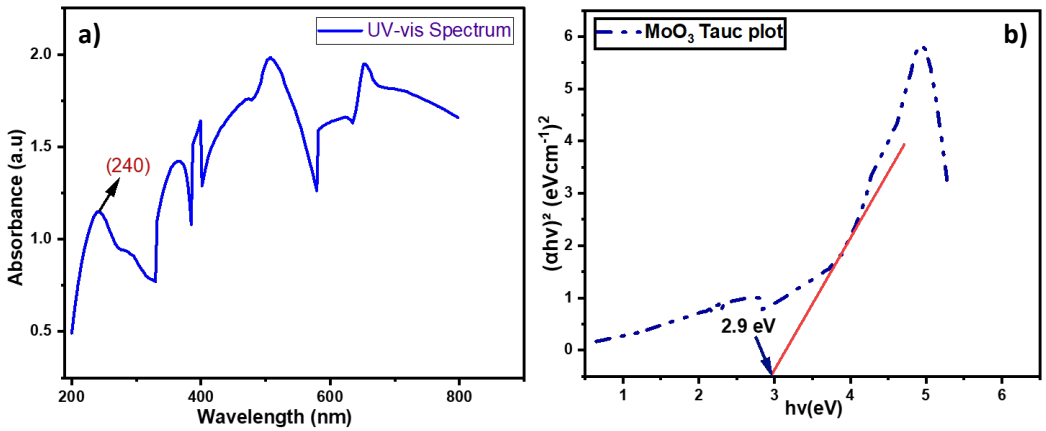

Fig. 3. a) UV absorbance spectrum of the synthesised MoO_3 NPs, b) Tauc plot of the synthesised MoO_3 NPs.

3.3 RAMAN

The Raman analysis of MoO3 NPs is illustrated in Figure 4. A strong peak ~900 cm-1 attributed to Mo = O stretching vibration, confirming the orthorhombic α-MoO3 phase. Peaks at

~820 cm-1 correspond to Mo-O-Mo stretching vibrations, indicating the layered Octahedral structure [23]. Weaker peaks ~666 cm-1 and ~472 cm-1 arise from stretching and bending vibrations of Mo-O-Mo in edge-sharing MoO6 octahedra of the orthorhombic MoO3 phase [26]. Low-frequency bands below ~ 200 cm-1 correspond to lattice vibrations or translational displacements of Mo atoms [27]. The observed Raman peaks and relative intensity are consistent with those previously reported. α-MoO3 nanostructures, minor shift or peak broadening may result from nanoscale structural defects or crystal lattice strain.

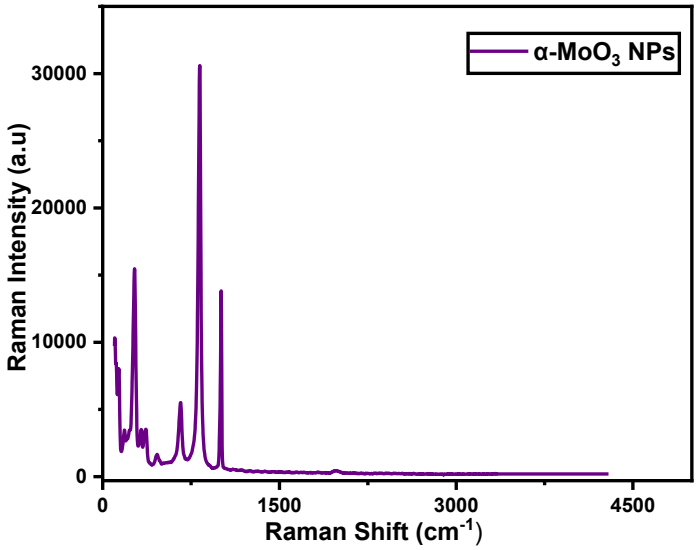

Fig. 4. RAMAN spectra of synthesised MoO_3 NPs.

3.4 SEM-EDAX

SEM analysis of the synthesised MoO3 NPs (Figure 5) reveals an irregular and porous morphology with agglomerated nanograins of diverse sizes. At lower magnification (5.00KX), the particles appear as loosely distributed clusters across the surface. Higher magnifications (10.00KX and 40.00KX) reveal plate-like and flake-shaped structures marked by rough surfaces. The agglomeration results from the high surface energy of the nanoparticle, which induces clustering during the process. Such morphology provides a greater surface-to-volume ratio, providing more active sites for photon absorption and ROS generation.

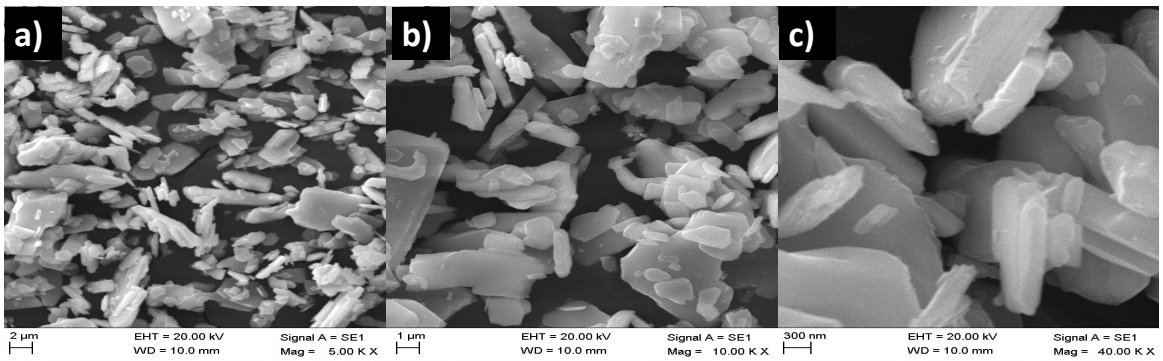

Fig. 5. SEM morphology of the synthesised MoO_3 NPs at different magnifications, a) 5.00KX, b)10.00KX C) 40.00KX.

The elemental composition of MoO3 NPs was further confirmed by the EDAX figure 6, which shows only Mo and O peaks. The absence of secondary peaks indicates the high phase purity of the sample.

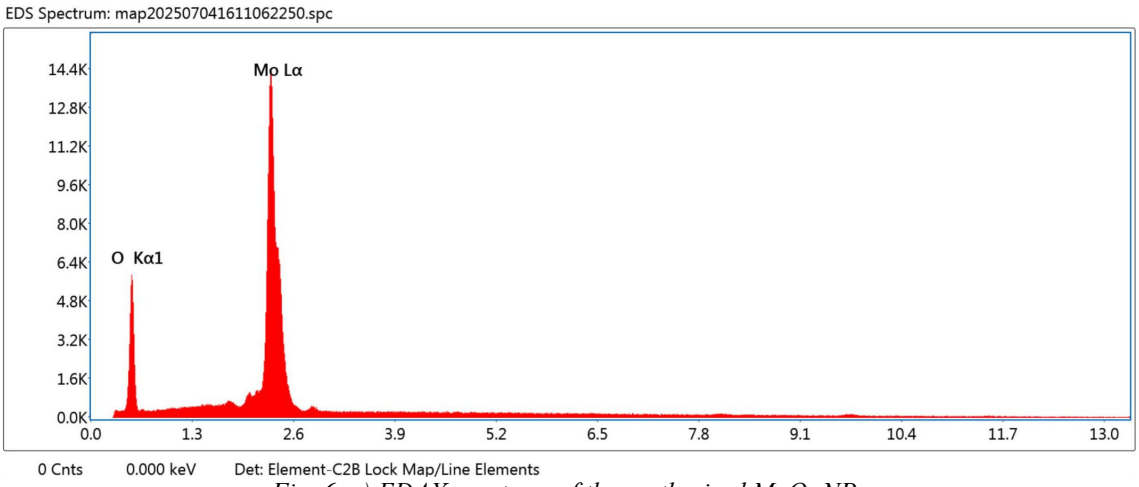

Fig. 6. a) EDAX spectrum of the synthesised MoO_3 NPs.

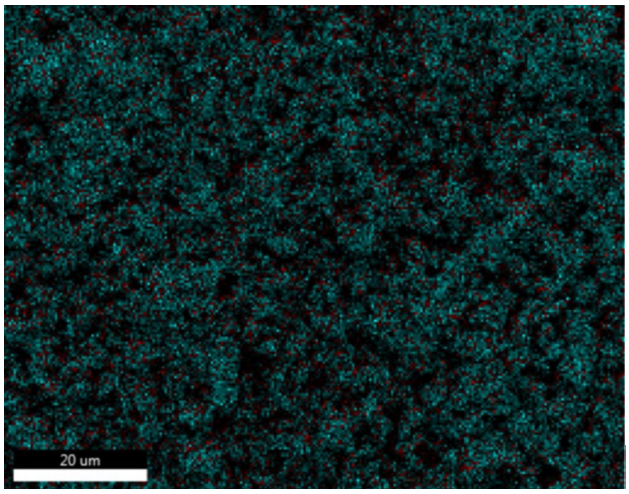

Fig. 6. b) Overlay plan view element map (EDAX) of the surface of the synthesised MoO_3 NPs. O = red, Mo = blue. Scale bar is 20 μm.

Table 1. Elemental analysis of MoO_3 NPs.

Element	Weight %	Atomic %	Error %	Kratio
O K	43.0	81.9	10.1	0.0762
MoL	57.0	18.1	1.7	0.5021

3.5 Photocatalytic activity

The photocatalytic activity of MoO3 NPs was performed under direct sunlight using MB dye. The dye concentration decreased progressively over time, reaching approximately 92 % removal within 120 minutes. The degradation kinetics obey the pseudo-first-order kinetic model, with a rate constant of k = 0.0185 min-1, as indicated by a linear trend, confirming consistent dye breakdown. One-way ANOVA revealed a significant increase in degradation efficiency with increasing irradiation time ($p < 0.05$).

The excellent photocatalytic performance of MoO3 NPs is attributed to their porous morphology and the ability of surface oxygen atoms, which facilitate the production of ROS (•OH, O2•-) responsible for dye degradation. The bandgap between 2.7- 3.0 eV enables efficient absorption of visible light, promoting electron-hole pair formation and enhancing photocatalytic activity [28]. These results demonstrate the potential of MoO3 NPs as effective photocatalysts for the degradation of agricultural residues [29].

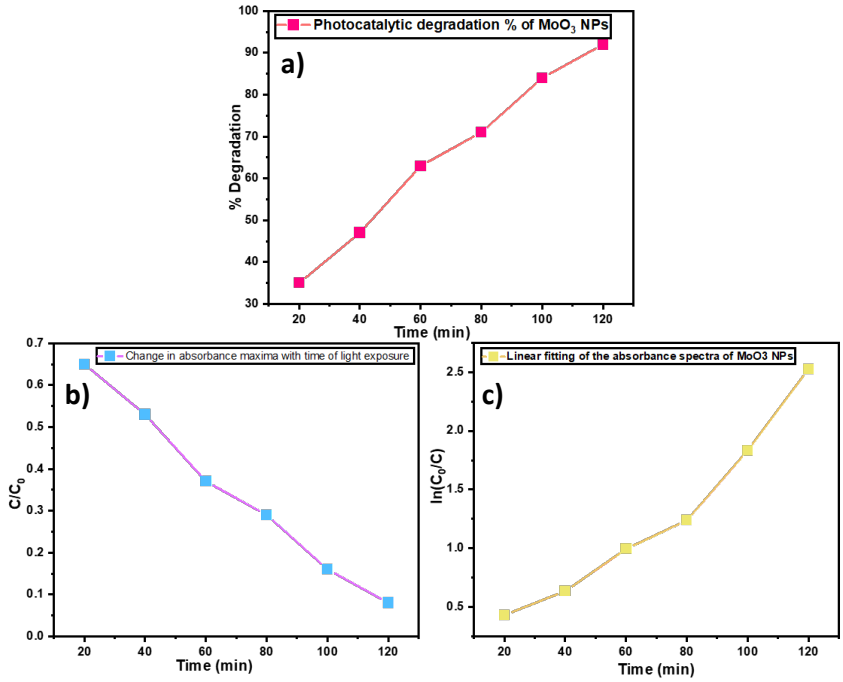

Figure 7. Degradation profile: a) Percentage degradation with time, b) Change in absorbance maxima with time of light exposure, c) Linear fitting of the absorbance spectra.

3.6 Antibacterial activity

Antibacterial properties were assessed using an agar well diffusion technique, wherein nutrient agar plates inoculated with Escherichia coli and Staphylococcus aureus were loaded at varying concentrations of the nanoparticles. The zone of inhibition is summarised in Table 2.

Table 2. Antibacterial activity of MoO_3 NPs against E. coli and S. aureus at different concentrations.

Bacteria	Concentration			+ve control	- ve control
	1 mg/ml	0.5 mg/ml	0.25 mg/ml		
Escherichia coli	17 ± 0.5^{a} mm	13 ± 0.4^{b} mm	9 ± 0.3^{c} mm	28 ± 0.7^{d} mm	NZ
Staphylococcus aureus	14 ± 0.4^{a} mm	11 ± 0.3^{b} mm	9 ± 0.2^{c} mm	27 ± 0.6^{d} mm	NZ

The findings reveal that the inhibition was concentration-dependent. The maximum Zone of inhibition was observed at higher concentrations, 1 mg/mL, measuring 17 ± 0.5 mm for E. coli and 14 ± 0.4 mm for S. aureus. At 0.5 mg/mL, the inhibition zones decreased to 13 ± 0.4 mm and 11 ± 0.3 mm, respectively, while at 0.25 mg/mL, the zones further reduced to 9 ± 0.3 mm for E. coli and 9 ± 0.2 mm for S. aureus ($p < 0.05$). The positive control (ciprofloxacin) exhibited significantly higher activity (28 ± 0.7 mm for E. coli and 27 ± 0.6 mm for S. aureus), while the negative control (NZ) showed no inhibition. These findings confirm the efficacy of MoO3 NPs as an eco-friendly antibacterial agent.

In addition to ROS-mediated toxicity, the antibacterial efficacy of MoO3 NPs is governed by their intrinsic acidity, as hydrated MoO3 can release molybdic acid (H2MoO4), leading to acidification of the surrounding environment [30]. Moreover, the release of Molybdate ions (MoO42-) disrupts essential enzymatic pathways, particularly those involved in nitrogen and sulfur metabolism, thereby impairing bacterial growth [31]. These combined mechanisms highlight the potential of MoO3 NPs as an eco-friendly and sustainable approach for controlling microbial contaminations in agricultural applications [32].

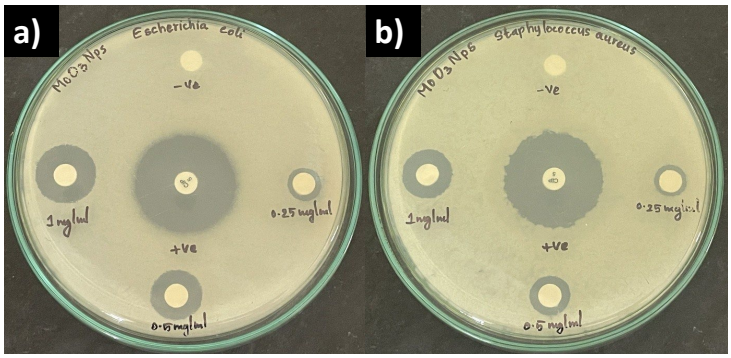

Figure 8. Antibacterial activity of synthesised MoO_3 NPs against a) E. coli and b) S. aureus at different concentrations.

4. Conclusion

Combustion-synthesised MoO3 NPs exhibited high crystallinity, visible-light activity, and dual functionality as photocatalysts and antibacterial agents. Their ability to degrade organic pollutants and inhibit pathogenic bacteria suggests strong potential for sustainable agricultural applications.

References

[1] S. Iravani, Green Chemistry **13**(10), 2638 (2011); https://doi.org/10.1039/C1GC15386B.
[2] M. S. S. Danish, L. L. Estrella, I. M. A. Alemaida, A. Lisin, N. Moiseev, M. Ahmadi, et al, Photocatalytic Applications of Metal Oxides for Sustainable Environmental Remediation **11**(1), 80 (2021); https://doi.org/10.3390/met11010080.
[3] A. Aboulouard, B. Gultekin, M. Can, M. Erol, A. Jouaiti, B. Elhadadi, et al, Journal of Materials Research and Technology **9**(2), 1569 (2020); https://doi.org/10.1016/j.jmrt.2019.11.083.
[4] S. Bhatia, N. Verma, Materials Research Bulletin **95**, 468 (2017); https://doi.org/10.1016/j.materresbull.2017.08.019.
[5] P. Silva, D. Cestarolli, E. Guerra, Optical Materials 117063 (2025); https://doi.org/10.1016/j.optmat.2025.117063.
[6] M. A. Hussein, M. M. Motawea, M. M. Elsenety, S. M. El-Bahy, H. Gomaa, Applied Nanoscience **12**(5), 1519 (2022); https://doi.org/10.1007/s13204-021-02318-0.
[7] M. G. da Silva Júnior, L. C. C. Arzuza, H. B. Sales, R. M. d. C. Farias, G. d. A. Neves, H. d. L. Lira, et al, A Brief Review of MoO3 and MoO3-Based Materials and Recent Technological Applications in Gas Sensors, Lithium-Ion Batteries, Adsorption, and Photocatalysis **16**(24), 7657 (2023); https://doi.org/10.3390/ma16247657.
[8] S. Yadav, J. Yadav, M. Kumar, K. Saini, International Journal of Hydrogen Energy **47**(99), 41684 (2022); https://doi.org/10.1016/j.ijhydene.2022.02.011.
[9] B. Elzein, Nano Revolution: “Tiny tech, big impact: How nanotechnology is driving SDGs progress **10**(10), (2024); https://doi.org/10.1016/j.heliyon.2024.e31393.
[10] J. Khan, S. Bibi, I. Naseem, S. Ahmed, M. Hafeez, K. Ahmed, et al, Ternary Metal (Cu–Ni–Zn) Oxide Nanocomposite via an Environmentally Friendly Route **8**(23), 21032 (2023); https://doi.org/10.1021/acsomega.3c01896.

[11] G. Murugadoss, K. Thiruppathi, N. Venkatesh, S. Hazra, A. Mohankumar, G. Thiruppathi, et al, Journal of Environmental Chemical Engineering **10**(1), 106961 (2022); https://doi.org/10.1016/j.jece.2021.106961.
[12] M. Ishfaq, W. Hassan, M. Sabir, H. Somaily, S. K. Hachim, Z. J. Kadhim, et al, Wet-chemical synthesis of ZnO/CdO/CeO2 heterostructure: A novel material for environmental remediation application International **48**(23), 34590 (2022); https://doi.org/10.1016/j.ceramint.2022.08.046.
[13] M. Mayakannan, S. Gopinath, S. Vetrivel, Materials Chemistry and Physics **242**, 122282 (2020); https://doi.org/10.1016/j.matchemphys.2019.122282.
[14] R. Verma, B. Balaji, A. Dixit, Phytochemical analysis and broad spectrum antimicrobial activity of ethanolic extract of Jasminum mesnyi Hance leaves and its solvent partitioned fractions **14**(8), 430 (2018); https://doi.org/10.6026/97320630014430.
[15] A. M. Taddesse, M. Alemu, T. Kebede, Journal of Environmental Chemical Engineering **8**(5), 104356 (2020); https://doi.org/10.1016/j.jece.2020.104356.
[16] A. Ashok, M. M. Al-Rawashdeh, L. Vechot, Process Safety and Environmental Protection 107476 (2025).
[17] J. Indrakumar, P. S. Korrapati, Biological Trace Element Research **194**(1), 121 (2020); https://doi.org/10.1007/s12011-019-01742-2.
[18] Z. Kalaycıoğlu, B. Özugur Uysal, O. Pekcan, F. B. Erim, Efficient Photocatalytic Degradation of Methylene Blue Dye from Aqueous Solution with Cerium Oxide Nanoparticles and Graphene Oxide-Doped Polyacrylamide **8**(14), 13004 (2023); https://doi.org/10.1021/acsomega.3c00198.
[19] A. W. Bauer, W. M. Kirby, J. C. Sherris, J. C. Turck, American Journal of Clinical Pathology **45**(4_ts), 493 (1966); https://doi.org/10.1093/ajcp/45.4_ts.493.
[20] P. C. Kohner, J. E. Rosenblatt, F. Cockerill 3rd, Journal of Clinical Microbiology **32**(6), 1594 (1994); https://doi.org/10.1128/jcm.32.6.1594-1596.1994.
[21] M. Mathabe, R. Nikolova, N. Lall, N. Nyazema, Journal of Ethnopharmacology **105**(1-2), 286 (2006); https://doi.org/10.1016/j.jep.2006.01.029.
[22] J. P. A. Assam, J. Dzoyem, C. Pieme, V. Penlap, BMC Complementary and Alternative Medicine **10**(1) 40 (2010); https://doi.org/10.1186/1472-6882-10-40.
[23] T. T. P. Pham, P. H. D. Nguyen, T. T. Vo, H. H. P. Nguyen, C. L. Luu, Advances in Natural Sciences: Nanoscience and Nanotechnology **6**(4), 045010 (2015); https://doi.org/10.1088/2043-6262/6/4/045010.
[24] A. Kumar, G. Pandey, American Journal of Nanosciences **3**(4), 81 (2017); https://doi.org/10.11648/j.ajn.20170304.12.
[25] S. Camacho-Lopez, M. Flores-Castañeda, M. Camacho-Segura, L. F. Devia-Cruz, N. Zamora-Romero, G. Aguilar, et al, Materials Chemistry and Physics **297**, 127376 (2023); https://doi.org/10.1016/j.matchemphys.2023.127376.
[26] M. Dieterle, G. Mestl, Physical Chemistry Chemical Physics **4**(5), 822 (2002); https://doi.org/10.1039/B107046K.
[27] L. Seguin, M. Figlarz, R. Cavagnat, J. C. Lassègues, Spectrochimica Acta Part A: Molecular and Biomolecular Spectroscopy **51**(8), 1323 (1995); https://doi.org/10.1016/0584-8539(94)00247-9.
[28] A. H. Alshammari, M. Alshammari, S. Alhassan, K. Alshammari, T. Alotaibi, T. A. M. Taha, Nanomaterials **13**(5), 820 (2023); https://doi.org/10.3390/nano13050820.
[29] Y. Liu, P. Feng, Z. Wang, X. Jiao, F. Akhtar, Scientific Reports **7**(1), 1845 (2017); https://doi.org/10.1038/s41598-017-02025-3.
[30] S. Shafaei, D. Van Opdenbosch, T. Fey, M. Koch, T. Kraus, J. P. Guggenbichler, et al, Materials Science and Engineering C **58**, 1064 (2016); https://doi.org/10.1016/j.msec.2015.09.069.
[31] T. N. Tikhonova, E. A. Shirshin, A. Y. Romanchuk, V. V. Fadeev, Colloids and Surfaces B: Biointerfaces **146**, 507 (2016); https://doi.org/10.1016/j.colsurfb.2016.06.049.
[32] C. Yin, H. Gu, S. Zhang, Journal of Cleaner Production **274**, 122867 (2020); https://doi.org/10.1016/j.jclepro.2020.122867.